






Cite this: DOI: 10.1039/c9ta11913b

Dual-phase MoS₂ as a high-performance sodium-ion battery anode†Junxiong Wu,^a Jiapeng Liu,^a ^a Jiang Cui,^a Shanshan Yao,^a Muhammad Ihsan-Ul-Haq,^a Nauman Mubarak,^a Emanuele Quattrocchi,^a Francesco Ciucci ^{*abc} and Jang-Kyo Kim ^{*a}

The increasing cost and limited availability of lithium have prompted the development of high-performance sodium-ion batteries (SIBs) as a potential alternative to lithium-ion batteries. However, it has been a critical challenge to develop high-performance anode materials capable of storing and transporting Na⁺ efficiently. Amongst the various options, MoS₂ has significant advantages including low cost, and a high theoretical capacity of ~670 mA h g⁻¹. Nevertheless, MoS₂ has several issues: its electronic conductivity is low and its structure deteriorates rapidly during charge/discharge cycles, leading to a poor electrochemical performance. Here, a dual-phase MoS₂ (DP-MoS₂) is synthesized by combining two distinct 1T (trigonal) and 2H (hexagonal) phases to solve these challenges. Compared to the conventional 2H-MoS₂ counterpart, the DP-MoS₂ phase material presents a highly reversible Na⁺ intercalation/extraction process aided by expanded interlayer spacing along with much higher electronic conductivity and Na ion affinity. Consequently, the DP-MoS₂ electrode delivers a high cyclic stability with a reversible capacity of 300 mA h g⁻¹ after 200 cycles at 0.5 A g⁻¹ and an excellent rate capability of ~220 mA h g⁻¹ at 2 A g⁻¹. The SIBs assembled with DP-MoS₂ and Na₃V₂(PO₄)₃ as the negative and positive electrodes, respectively, have a specific capacity of 210 mA h g⁻¹ (based on the mass of DP-MoS₂) at 0.5 A g⁻¹. This performance demonstrates that DP-MoS₂ has a significant potential in commercial devices. This work offers a new approach to develop metal chalcogenides for electrochemical energy storage applications.

Received 30th October 2019
Accepted 1st January 2020

DOI: 10.1039/c9ta11913b

rsc.li/materials-a

1. Introduction

Lithium-ion batteries (LIBs) have been the predominant rechargeable devices powering portable electronics and electric vehicles because of their high energy densities and long cycle life.^{1–4} Two of the main concerns surrounding LIBs lie in the rapidly rising material costs and limited resources of lithium, which have prompted the search for low-cost alternatives.⁵ As a potential alternative, sodium-ion batteries (SIBs) have attracted significant interest because of the natural abundance and low costs of Na precursors.^{6–8} However, the larger ionic radius and heavier molar mass of Na⁺ result in sluggish reaction kinetics, inevitably leading to lower specific capacities, inferior cyclic stability, and poorer rate capabilities than LIBs.⁹ Also, graphite – the most commonly used anode material for LIBs – is unsuitable for Na⁺ intercalation due to the insufficient

interlayer spacing and unfavorable thermodynamics.^{10–12} Therefore, developing suitable host materials with efficient Na⁺ storage and transport is critical to achieve energy densities and cyclic stabilities to the levels of current LIBs.

As a typical layered transition metal dichalcogenide (TMD), whose monolayer consists of two close-packed chalcogenide planes sandwiching a transition metal layer, MoS₂ is a promising anode material for SIBs.^{13,14} Its notable advantages include a unique layered structure, low cost, and a high theoretical capacity of ~670 mA h g⁻¹.^{15,16} However, most reported MoS₂-based anodes to date are in the hexagonal (2H) phase, which has a low intrinsic electronic conductivity and whose structure tends to deteriorate during repeated charge/discharge cycles, leading to poor cyclic stability.¹⁷ A typical strategy to ameliorate the structural stability and electronic conductivity of MoS₂ is to combine with a carbon matrix assembling MoS₂/C composites.^{11,18–22} For example, a sandwich structure was assembled using MoS₂ coupled with porous graphene sheets so that the electron transport networks ensured structural stability against volume changes during charge/discharge cycles.²⁰ Another effective approach is to control the cut-off voltage *versus* Na/Na⁺.^{11,16,23} It is found that MoS₂ underwent an intercalation reaction rather than a conversion reaction between 0.4 and 3 V *vs.* Na/Na⁺.¹⁶ The intercalation/extraction chemistry is highly

^aDepartment of Mechanical and Aerospace Engineering, The Hong Kong University of Science and Technology, Clear Water Bay, Kowloon, Hong Kong, China. E-mail: francesco.ciucci@ust.hk; mejkkm@ust.hk

^bDepartment of Chemical and Biological Engineering, The Hong Kong University of Science and Technology, Clear Water Bay, Hong Kong, China

^cGuangzhou HKUST Fok Ying Tung Research Institute, China

† Electronic supplementary information (ESI) available. See DOI: 10.1039/c9ta11913b

reversible, and the layered structure of MoS₂ can be retained even after long-term cycle tests.

Benefitting from different coordination between Mo and S atoms, the trigonal (1T) phase MoS₂ has a much higher electronic conductivity than the semiconducting 2H counterpart.²⁴ This unique structural feature makes 1T MoS₂ an emerging electrode material for batteries,^{25–28} supercapacitors,^{24,29} and catalysts.^{30–32} Compared to the stable 2H phase, however, 1T MoS₂ is metastable by nature and can be easily converted into the 2H phase by oxidation.³³ An effective approach to obtain 2D MoS₂ with a high fraction of the 1T phase is the intercalation of alkali metal ions into MoS₂ flakes followed by exfoliation.^{34,35} However, this method is complicated and hazardous because highly flammable *n*-butyl lithium needs to be used as the reaction agent.^{34,35} Recently, the 1T-MoS₂ was stabilized by inserting NH₄⁺ molecules using a facile solvothermal method, which was used in supercapacitors or for the evolution of hydrogen.^{36,37} Meanwhile, only a few reports have so far demonstrated the potential of 1T-MoS₂ as an anode for LIBs or SIBs.^{25–28,38} For example, freestanding metallic MoS₂ was grown on a graphene foam to serve as an anode for SIBs with a reversible specific capacity of 313 mA h g^{−1} after 200 cycles.²⁸ However, its cyclic stability and rate capability were rather poor because the deep charge/discharge cycles took place in the voltage range from 0.005 to 3 V vs. Na/Na⁺.

Herein, we synthesized a dual-phase MoS₂ (DP-MoS₂) by a facile solvothermal method, which was used for the storage of Na. If the cut-off voltage remained between 0.4 and 3 V vs. Na/Na⁺, the DP-MoS₂ electrode underwent highly reversible Na⁺ intercalation/extraction cycles, as supported by *ex situ* X-ray photoelectron spectroscopy (XPS) and transmission electron microscopy (TEM) analyses. The theoretical simulations indicate that Na atoms more favorably absorbed and diffused in DP-MoS₂ than in 2H-MoS₂. The DP-MoS₂ electrode delivers a reversible capacity of 300 mA h g^{−1} after 200 cycles at 0.5 A g^{−1} along with an excellent rate capability of ~220 mA h g^{−1} at 2 A g^{−1}. A 2.5 V prototype full cell composed of the DP-MoS₂ anode and a Na₃V₂(PO₄)₃ (NVP) cathode retains an excellent specific capacity of 168 mA h g^{−1} after 100 cycles, corresponding to a capacity retention rate of ~80%.

2. Experimental section

2.1 Material preparation

DP-MoS₂ was synthesized through a facile solvothermal method in a mixture of dimethylformamide (DMF) and deionized water (v/v = 3 : 2). Specifically, 1.5 mmol sodium molybdate (Na₂MoO₄) and 5 mmol L-cysteine were dissolved in 70 mL mixed solution under continuous stirring. The solution was then transferred to a 100 mL Teflon-lined autoclave, which was maintained at 200 °C for 12 h. After cooling to room temperature, the obtained black DP-MoS₂ powders were thoroughly washed with ethanol and dried in a vacuum oven at 60 °C overnight. For comparison, the 2H-MoS₂ was obtained by annealing DP-MoS₂ at 700 °C for 3 h under N₂ flow.

2.2 Structural and morphological characterization

The XRD patterns were obtained on a Philips PW1830 diffractometer with Cu K α radiation. The morphologies of materials were examined by scanning electron microscopy (SEM) (JSM-6700F, JEOL) and TEM (FEI TECNAI G2 F30). The Raman spectra were collected using a Raman spectrometer (HORIBA Labram HR Evolution) equipped with a 532 nm Ar-ion laser. The UV-vis spectra were collected on a SEC2000 UV-visible spectrophotometer (ALS Co., Ltd.). The XPS spectra were recorded using an ESCALAB 250Xi (Thermo Fisher) with a monochromatic Al K α source. Nitrogen adsorption/desorption isotherms and Brunauer–Emmett–Teller (BET) surface area were obtained using a Micromeritics ASAP 2020 analyzer. The electrical conductivities of DP-MoS₂ and 2H MoS₂ were measured on a four-probe resistivity/Hall system (HK5500PC, Bio-Rad). For the *ex situ* XPS and TEM characterizations, the coin cells were first disassembled in an Ar-filled glove box (Mbraun), and the electrodes were then thoroughly washed with dimethyl carbonate (DMC).

2.3 Electrochemical measurements

The working electrode was composed of the active material, either DP-MoS₂ or 2H-MoS₂, carbon black, and sodium carboxymethyl cellulose binder at a weight ratio of 7 : 2 : 1. The homogeneously mixed slurry was coated onto a thin Cu foil and dried at 80 °C in a vacuum oven for 12 h. Subsequently, the electrodes were punched into circular discs of 12 mm in diameter. The typical loading of the active materials was 1.0–1.2 mg cm^{−2}, a value consistent with literature reports.^{18,27} The CR2032-type coin cells were assembled in an Ar-filled glove box using Na metal foil as the counter electrode and glass microfiber (Whatman, GF/D) as the separator. 1 M NaCF₃SO₃ in diglyme and 1 M NaClO₄ in propylene carbonate (PC) with 5 vol% fluoroethylene carbonate (FEC) were chosen as the electrolyte. The galvanostatic charge/discharge (GCD) tests were conducted on a battery testing system (Land 2001CT) over a potential range from 0.4 to 3.0 V. Galvanostatic intermittent titration technique (GITT) measurements were carried out by applying a constant current of 100 mA g^{−1} for 10 minutes followed by a 4 h relaxation to reach equilibrium. Cyclic voltammetry (CV) tests were performed at a scan rate of 0.1 mV s^{−1} in the same voltage range on an electrochemical workstation (CHI 660C). Electrochemical impedance spectroscopy (EIS) measurements were conducted in the range of frequency from 10 mHz to 100 kHz on the same workstation.

Na-ion full cells were assembled using the DP-MoS₂ anode and an NVP cathode at an anode to cathode mass ratio of 1 : 4. The cathode slurry was prepared by mixing NVP with carbon black and polyvinylidene difluoride (PVDF) binder at a weight ratio of 8 : 1 : 1 in *N*-methyl pyrrolidone (NMP) solvent. The NVP electrode was fabricated by coating the mixed slurry on the carbon-coated Al current collector. The specific capacities of batteries were calculated based on the mass of DP-MoS₂ or 2H-MoS₂.

2.4 Theoretical calculations

All spin-polarized density functional theory (DFT) calculations were performed under the general gradient approximation (GGA) using the Perdew–Burke–Ernzerhof (PBE) functionals as implemented in the Vienna *ab initio* simulation package (VASP).^{39,40} The core and valence electronic interactions were treated with the projector augmented wave method. The van der Waals (vdW) interaction between the MoS₂ layers was corrected using the vdW-D3 method.⁴¹ The kinetic cutoff for plane-waves was set at 500 eV, and $5 \times 5 \times 3$ Monkhorst–Pack grids were used. 2×2 supercells with the Mo₈S₁₆ composition were modeled. The force convergence criterion was set at $0.02 \text{ eV } \text{\AA}^{-1}$. The binding energy per Na atom, E_{binding} , of DP-MoS₂ and 2H-MoS₂ is defined as⁴²

$$E_{\text{binding}} = \frac{E_{\text{MoS}_2 + n\text{Na}} - E_{\text{MoS}_2} - nE_{\text{Na}}}{n} \quad (1)$$

where $E_{\text{MoS}_2 + n\text{Na}}$ is the total energy of sodiated structures with n Na atoms intercalated, E_{MoS_2} is the energy of MoS₂ alone without Na, and E_{Na} is the energy of a single Na atom in the Na crystal. We also performed *ab initio* molecular dynamics (AIMD) simulations at 600 K in an NVT ensemble with the Nosé thermostat to control the temperature.⁴³ For the MD simulations, the same 500 eV kinetic cutoff was used and the Brillouin zone was sampled on a Γ -centered $1 \times 1 \times 1$ k -point grid. The total simulation time was 30 ps with a step of 2 fs. The mean-squared displacement (MSD) of Na was calculated using the following expression:⁴⁴

$$\text{MSD}(\Delta t) = \frac{1}{n} \sum_{i=1}^n |r_i(t + \Delta t) - r_i(t)|^2 \quad (2)$$

where n is the total number of Na atoms in the MoS₂ supercell.

3. Results and discussion

3.1 Properties of DP-MoS₂

The morphology and structure of DP-MoS₂ were examined by SEM, TEM, and high-resolution TEM (HRTEM), as shown in Fig. 1. The size of DP-MoS₂ particles was 250–300 nm (Fig. 1a and b), and the interlayer spacing was $\sim 9.4 \text{ \AA}$ (Fig. 1c). The HRTEM image (Fig. 1d) verifies the coexistence of both the 1T and 2H phases in DP-MoS₂. As revealed by different coordination modes of MoS₂ (rightmost side of Fig. 1d), the red square area with a symmetrical Mo arrangement illustrates the presence of 1T-MoS₂, whereas the yellow square area with a symmetrical Mo–Mo spacing surrounded by 3 S atoms indicates the existence of 2H-MoS₂.^{36,45} The scanning transmission electron microscopy (STEM) image and the corresponding energy dispersive X-ray (EDX) spectrum shown in Fig. 1e confirm the uniform distribution of Mo and S atoms throughout DP-MoS₂. The 2H-MoS₂ particles had a size and morphology similar to those of DP-MoS₂ (Fig. S1a and b†). The TEM image (Fig. S1c†) presents an interlayer spacing $\sim 6.3 \text{ \AA}$ of 2H-MoS₂. The HRTEM image (Fig. S1d†) displays the characteristic atomic arrangement of 2H-MoS₂, indicating the

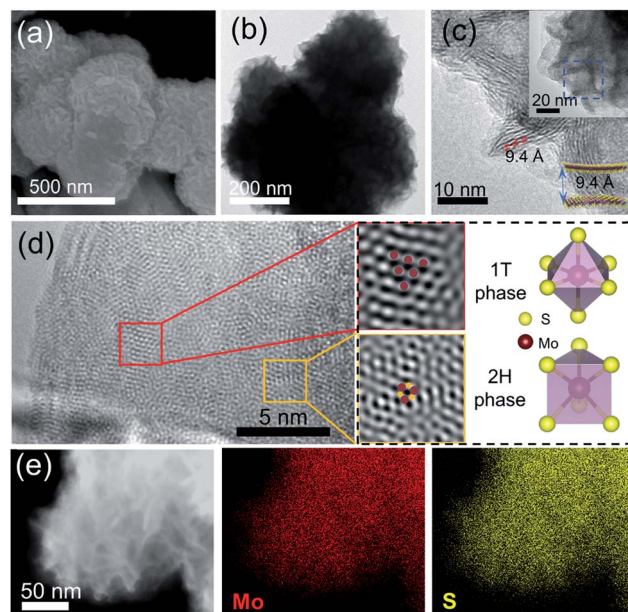


Fig. 1 (a) SEM, (b) TEM, (c and d) HRTEM images and (e) STEM-EDX maps of DP-MoS₂.

transformation from the dual phase to the pure 2H phase after annealing.⁴⁶

The X-ray diffraction (XRD) patterns of DP-MoS₂ and 2H-MoS₂ are presented in Fig. 2a. The 2H-MoS₂ displays three major diffraction peaks at around 13.7° , 33.2° , and 58.7° , which can be assigned to the (002), (100), and (110) planes, respectively. In contrast, DP-MoS₂ has a (002) diffraction peak at $\sim 9.4^\circ$ corresponding to an interplanar distance of 9.4 \AA , in agreement with the TEM result (Fig. 1c). The enlarged interlayer of DP-MoS₂ is a reflection of the intercalation of S–Mo–S layers by the $\text{NH}_3/\text{NH}_4^+$ species generated during the solvothermal synthesis.^{36,37}

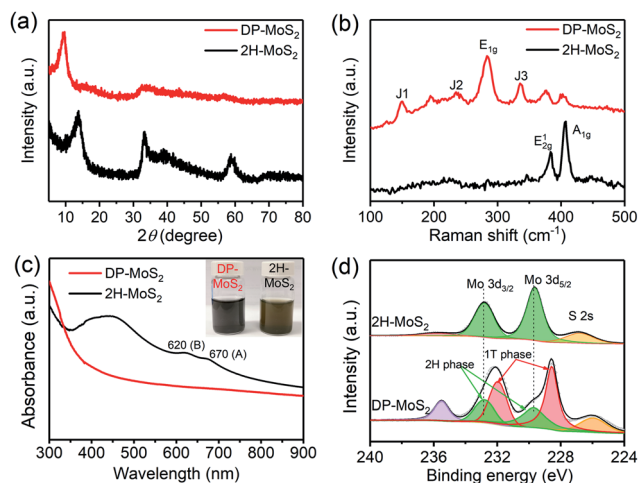


Fig. 2 (a) XRD patterns, (b) Raman spectra, and (c) UV-vis spectra of DP-MoS₂ and 2H-MoS₂. The inset of (c) shows a photograph of the DP-MoS₂ and 2H-MoS₂ suspensions in water. (d) Deconvoluted Mo 3d XPS spectra of DP-MoS₂ and 2H-MoS₂.

The Raman spectra (Fig. 2b) of DP-MoS₂ had the typical E_{1g} mode of 1T phase at 283 cm⁻¹. Three additional peaks located at 148 (J₁), 234 (J₂), and 335 (J₃) cm⁻¹ also confirm the presence of the 1T phase.^{25,29} In contrast, 2H-MoS₂ had only two sharp peaks at 383 and 406 cm⁻¹, which can be attributed to the E_{2g}¹ and A_{1g} modes of 2H phase MoS₂, respectively.^{18,47,48} We noticed that DP-MoS₂ also had two small peaks characteristic of 2H-MoS₂, supporting the concurrence of 2H and 1T phases in this material. The UV-visible absorption spectra of DP-MoS₂ and 2H-MoS₂ dispersions were also measured to distinguish the phases in two materials, as shown in Fig. 2c. The 2H-MoS₂ possessed two excitonic peaks (A and B) at 620 and 670 nm, indicating semiconducting characteristics. These two peaks disappeared in DP-MoS₂ due to its metallic nature, consistent with previous reports.^{27,49–51} The optical images in the inset of Fig. 2c also confirm the presence of different phases in the DP-MoS₂ and 2H-MoS₂ by showing that the 2H-MoS₂ dispersion was yellow-green while the 1T-MoS₂ counterpart was dark grey.^{27,50}

The XPS spectra also support the above findings for DP-MoS₂, as shown in Fig. 2d. The deconvoluted Mo 3d spectrum of 2H-MoS₂ showed two prominent peaks at 232.8 and 229.6 eV, corresponding to Mo 3d_{3/2} and Mo 3d_{5/2}, respectively.⁴⁸ The spectrum of DP-MoS₂ exhibit two characteristic doublets. The peaks in the first doublet at 232.0 and 228.7 eV can be attributed to the Mo 3d_{3/2} and Mo 3d_{5/2} peaks of the 1T phase,¹⁹ while the

peaks in the other doublet at 232.8 and 229.6 eV correspond to the Mo 3d_{3/2} and Mo 3d_{5/2} peaks of the 2H phase. This observation is consistent with the coexistence of both 1T and 2H phases. According to the XPS peak deconvolution, the fraction of 1T phase in DP-MoS₂ was ~62.5%. It is worth noting that the S 2p_{3/2} and 2p_{1/2} peaks of DP-MoS₂ exhibited similar down shifts (Fig. S2a) as a result of the presence of metallic 1T phase.²⁵ A new peak appeared at 401.7 eV in the N 1s spectrum of DP-MoS₂ (Fig. S2b†), suggesting the intercalation of NH₄⁺.³⁷

The BET surface area of DP-MoS₂ was 13.2 m² g⁻¹, a value 65% larger than that of 2H-MoS₂, see Fig. S3a.† The pore size distribution calculated by the Barrett-Joyner-Halenda (BJH) method indicates the hierarchical porous structure in DP-MoS₂ (Fig. S3b†). The large surface area and mesoporous structure favor the transport of electrons and ions and ultimately benefits high rate performance.⁵² The electrical conductivities measured using the 4-probe method at room temperature were 9.8 S m⁻¹ and 1.2 × 10⁻³ S m⁻¹ for DP-MoS₂ and 2H-MoS₂, respectively, in agreement with the literature.⁴⁹ The higher electrical conductivity of DP-MoS₂ is expected to boost the battery performance, especially at high rates.

3.2 Electrochemical performance

CV measurements were carried out to investigate the fundamental Na⁺ storage behavior of the MoS₂ electrodes assembled without adding carbon or binder for a pure system. For 2H-

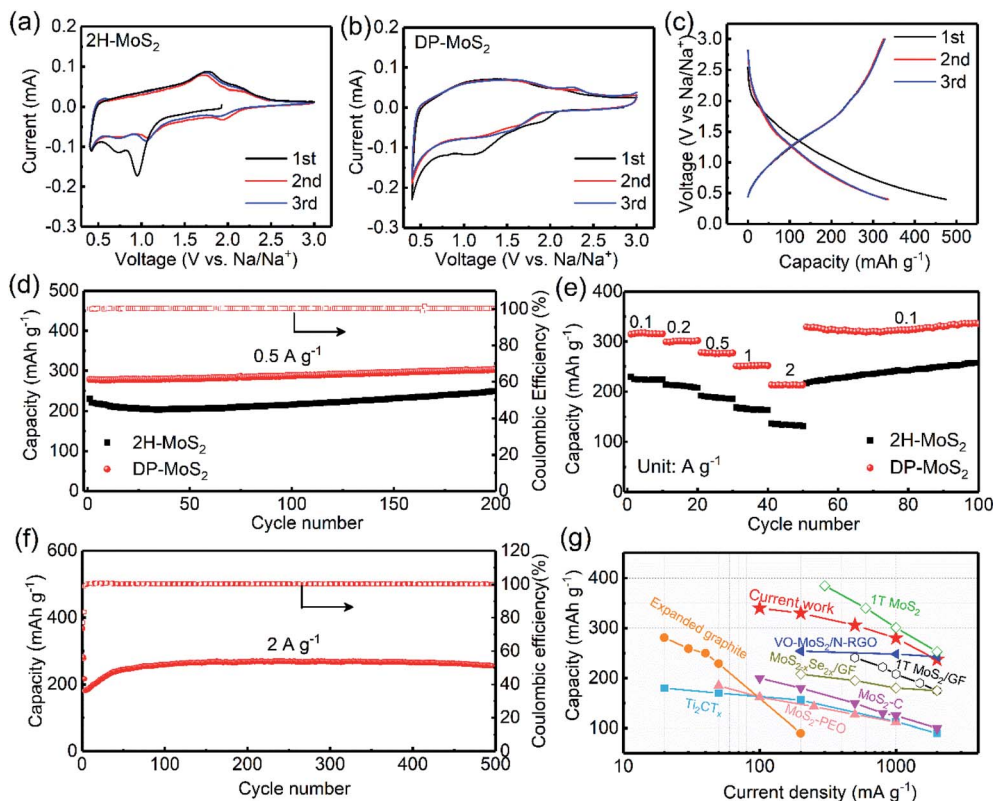


Fig. 3 CV curves of (a) the 2H-MoS₂ and (b) DP-MoS₂ electrodes; (c) GCD curves of the DP-MoS₂ electrode for the first three cycles at 0.1 A g⁻¹; (d) cyclic performance and (e) rate capability of the DP-MoS₂ and 2H-MoS₂ electrodes; (f) long-term cyclic performance of the DP-MoS₂ electrode at 2 A g⁻¹; (g) electrochemical performance of published SIB anodes compared with the current work.

MoS₂, two sharp cathodic peaks appeared at 0.95 and 0.70 V (Fig. 3a) and are ascribed to the intercalation of Na⁺ into the 2H phase MoS₂.⁵³ In contrast, DP-MoS₂ exhibited poorly-defined peaks relative to 2H-MoS₂ without any peaks at 0.95 V in the first cathodic scan (Fig. 3b), indicating no phase transformation during the intercalation of Na⁺ into DP-MoS₂. The CV curves for the second scan and onwards almost overlapped, suggesting highly reversible cyclic performance.

The first three GCD profiles of the DP-MoS₂ electrode (Fig. 3c) present initial discharge and charge capacities of 468 and 330 mA h g⁻¹, respectively, with an initial Coulombic efficiency (CE) of 68%. The capacity loss in the first cycle was probably triggered by the formation of a solid-electrolyte interface (SEI) film.^{18,52} After the first cycle, the CE became and remained higher than 99%, indicating a good electrochemical reversibility of the electrode. Fig. 3d reports the cyclic performances of the two electrodes at 0.5 A g⁻¹, which were activated at 0.1 A g⁻¹ for 3 cycles. The initial charge capacities were 280 and 220 mA h g⁻¹ for the DP-MoS₂ and 2H-MoS₂ electrodes, respectively. It is worth noting that the DP-MoS₂ electrode maintained a capacity of almost 300 mA h g⁻¹ without decay for the whole 200 cycles, showing excellent cyclic stability. The capacity of the 2H-MoS₂ electrode initially decreased until about 50 cycles. Beyond that point, it reversed its trend to increase continuously for the rest of the 200 cycles. A similarly abnormal phenomenon has been observed previously for transition metal compounds,^{25,54} for which the reversible formation of organic polymeric/gel-like layers by electrolyte decomposition and the activation of the electrode material led to a gradual increase in capacity.^{55,56} The rate performance of the electrodes are shown in Fig. 3e, and the corresponding GCD curves are given in Fig. S4.† The DP-MoS₂ cell delivered reversible capacities of 320, 300, 280, 255, and 220 mA h g⁻¹ at 0.1, 0.2, 0.5, 1, and 2 A g⁻¹, respectively. These values were significantly higher than those of the 2H-MoS₂ cell, namely, 220, 210, 200, 170, and 145 mA h g⁻¹, respectively. The DP-MoS₂ electrode also delivered a high charge capacity of 220 mA h g⁻¹ after 500 cycles at 2 A g⁻¹ along with ~100% CE, as shown in Fig. 3f.

To demonstrate the potential of DP-MoS₂ as an anode material for practical SIBs, its Na storage performance is compared with those of other state-of-the-art anode materials,^{11,27,28,53,57–60} as shown in Fig. 3g. The capacities vs. current density of the present DP-MoS₂ anode are higher than the majority of the reported anode materials, except the 1T-MoS₂ anode. The slightly higher capacity of 1T-MoS₂ nanosheets may be explained by the high 1T phase fraction of ~70% and the lower cut-off potential of 0.01 V vs. Na/Na⁺. However, it should be noted that the 1T-MoS₂ nanosheet electrode delivered a much lower initial CE of 60% and poorer capacity retention of 94% after only 200 cycles than the DP-MoS₂ counterpart. Apart from the performance, the Li⁺ ion intercalation-assisted exfoliation method used to prepare the 1T-MoS₂ nanosheets is inefficient and always introduces residues of foreign ions into the as-prepared MoS₂ nanosheets.¹³ The detailed data used in the comparison are shown in Table S2.† Considering the full-cell performance of DP-MoS₂//NVP batteries, the DP-MoS₂ has

a significant potential in commercial devices (see details in Section 3.4).

It should be pointed out that the electrolyte also played an important role in determining the electrochemical performance of the DP-MoS₂ electrode (Fig. S5†). The cyclic stability of the DP-MoS₂ electrode significantly improved when the ether-based electrolyte (*i.e.* 1 M NaCF₃SO₃ in diglyme) was used in place of the carbonate-based electrolyte (*i.e.* 1 M NaClO₄ in PC with 5 vol% FEC). The above finding signifies that the use of ether-based electrolyte ensured the formation of a stable SEI film, which in turn avoided the consumption of electrolyte during repeated cycles. In addition, we measured the cyclic performance of both DP-MoS₂ and 2H-MoS₂ electrodes at 0.5 A g⁻¹ for potentials (*vs.* Na) from 0.01 to 3.0 V. As shown in Fig. S6,† the DP-MoS₂ electrode had a capacity of nearly 440 mA h g⁻¹ corresponding to a retention of ~92% at the 100th cycle. In contrast, the capacity of the 2H-MoS₂ electrode decreased sharply after the 70th cycle. The improved cyclic performance of DP-MoS₂ can be attributed to the enhanced capability of 1T-MoS₂ to suppress the release and dissolution of S species over 2H-MoS₂.^{27,45} It is worth noting that the cyclic performance of DP-MoS₂ tested between 0.01 and 3.0 V was worse than the one assessed between 0.4 and 3 V, especially after 100 cycles. This may due to the structural degradation at low voltages (below 0.4 V *vs.* Na/Na⁺), where the 1T-Na_xMoS₂ is decomposed into Mo and Na₂S.¹⁶

The intercalation reaction of Na//DP-MoS₂ was probed by *ex situ* XPS in the voltage window between 0.4 and 3 V *vs.* Na/Na⁺, as shown in Fig. S7a.† When the DP-MoS₂ cell was discharged to 1.6 V, both the 1T and 2H phases of MoS₂ coexisted. Upon discharging to 0.4 V, however, only the 1T-MoS₂ phase remained, suggesting phase transition from 2H to 1T triggered by Na⁺ intercalation. When the cell was recharged to 3 V, the 2H-MoS₂ phase reappeared, indicating a reversible intercalation/extraction as supported also by the overlapped CV curves (Fig. 3b). Further, we recorded *ex situ* HRTEM images of the DP-MoS₂ electrode after discharging to 0.4 V in the 100th cycle (Fig. S7b†). It is clear that the DP-MoS₂ anode remained crystallographically layered with no fragmented Mo particles. These findings support the idea that the intercalation storage mechanism was dominant when the voltage was cut-off at 0.4 V in the Na//DP-MoS₂ battery.

To investigate the energy storage kinetics, the diffusion coefficient of Na⁺ (D_{Na^+}) was estimated using the GITT within the voltage window of 0.4–3 V. Fig. 4a shows the GITT curves of DP-MoS₂ and 2H-MoS₂ obtained after activation. During the GITT measurements, the cells were discharged/charged at 100 mA g⁻¹ for 10 min, followed by a relaxation for 4 h to reach the steady-state voltages (Fig. 4b). The D_{Na^+} was obtained using the formula:⁶¹

$$D_{\text{Na}^+} = \frac{4}{\pi\tau} \left(\frac{m_{\text{B}} V_{\text{M}}}{M_{\text{B}} S} \right)^2 \left(\frac{\Delta E_{\text{s}}}{\Delta E_{\text{t}}} \right)^2 \quad (3)$$

where τ denotes the constant current pulse time; m_{B} , M_{B} , and V_{M} are the mass, molar weight, and molar volume of the active materials, respectively. S is the total contact area between the

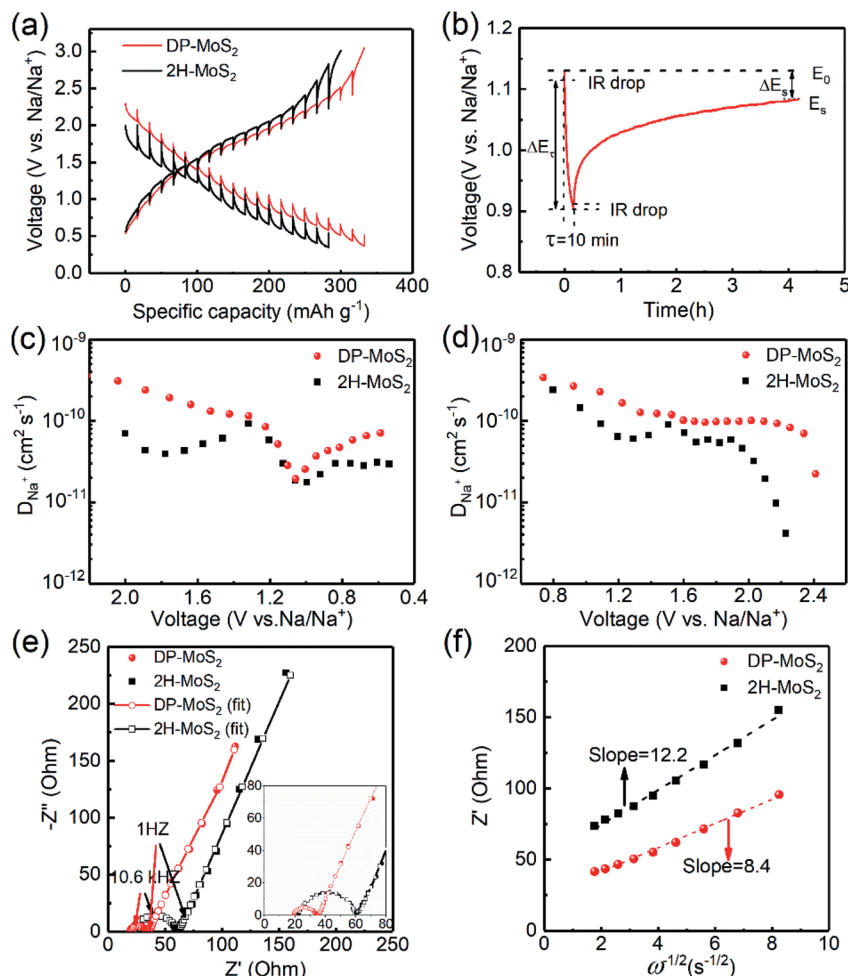


Fig. 4 (a) GITT potential profiles of DP-MoS₂ and 2H-MoS₂, (b) a single step of a GITT experiment. Na⁺ diffusion coefficients calculated from GITT potential profiles during (c) sodiation and (d) desodiation. (e) Nyquist plots and (f) plots of $\omega^{-1/2}$ versus Z' of DP-MoS₂ and 2H-MoS₂.

electrolyte and the electrode. ΔE_s and ΔE_t are the changes in steady-state voltage after subtracting the I_R drop and the total transient change in cell voltage during a single titration. The D_{Na^+} values are plotted as a function of cell voltage during both discharge and charge processes, as shown in Fig. 4c and d, respectively. The DP-MoS₂ electrode generally presented higher D_{Na^+} values than the 2H-MoS₂ counterpart in both the charge and discharge cycles. The D_{Na^+} values for DP-MoS₂ were in a range of 2.23×10^{-11} to $3.60 \times 10^{-10} \text{ cm}^2 \text{ s}^{-1}$, which are on par or much higher than those reported previously for SIB anode materials using the same GITT method: for example, 10^{-10} to $10^{-15} \text{ cm}^2 \text{ s}^{-1}$ for NaTi₂(PO₄)₃,⁶² 10^{-11} to $9 \times 10^{-11} \text{ cm}^2 \text{ s}^{-1}$ for rice husk-derived hard carbon anodes,⁶³ 4.26×10^{-14} to $1.42 \times 10^{-10} \text{ cm}^2 \text{ s}^{-1}$ for CuS,⁶⁴ and 10^{-11} to $10^{-14} \text{ cm}^2 \text{ s}^{-1}$ for Fe₂(SO₄)₃.⁶⁵ The highly intrinsic electronic conductivity of DP-MoS₂ is partly responsible for the high Na⁺ diffusion rate, which also contributed to its good rate capability.

The EIS spectra obtained after 100 cycles at 0.5 A g^{-1} are shown in Fig. 4e. The equivalent circuit model given in Fig. S8† was used to fit the EIS curves and the impedance parameters determined thereby are given in Table S1.† The charge transfer

resistance, R_{ct} , values of the DP-MoS₂ and 2H-MoS₂ electrodes were 13.8Ω and 31.3Ω , respectively, consistent with the much higher electrical conductivity of the former. The EIS spectra were further analyzed using a model based on the non-linear distribution of diffusion times (NL-DDT).⁶⁶ The experimental impedance curves were well fitted over the entire frequency range, giving estimated D_{Na^+} values of 7.3×10^{-11} and $3.9 \times 10^{-11} \text{ cm}^2 \text{ s}^{-1}$, respectively, for the DP-MoS₂ and 2H-MoS₂ electrodes (Fig. S9†). These D_{Na^+} values are of the same order as those estimated by GITT. The Z' versus $\omega^{-1/2}$ ($\omega = 2\pi f$) curves in the low-frequency region are shown in Fig. 4f. The lower slope value of the former than the latter electrode, i.e. 8.4 vs. 12.2, agrees well with the lower R_{ct} and the higher D_{Na^+} of the DP-MoS₂ electrode.

3.3 Theoretical analysis

DFT calculations were performed to elucidate the root causes of electrochemical performance of DP-MoS₂. The interlayer spacing of 1T-MoS₂ and 2H-MoS₂ models were set at 9.4 \AA and 6.3 \AA , respectively, according to the XRD and TEM results. The number of Na atoms accommodated by the MoS₂ lattice varied

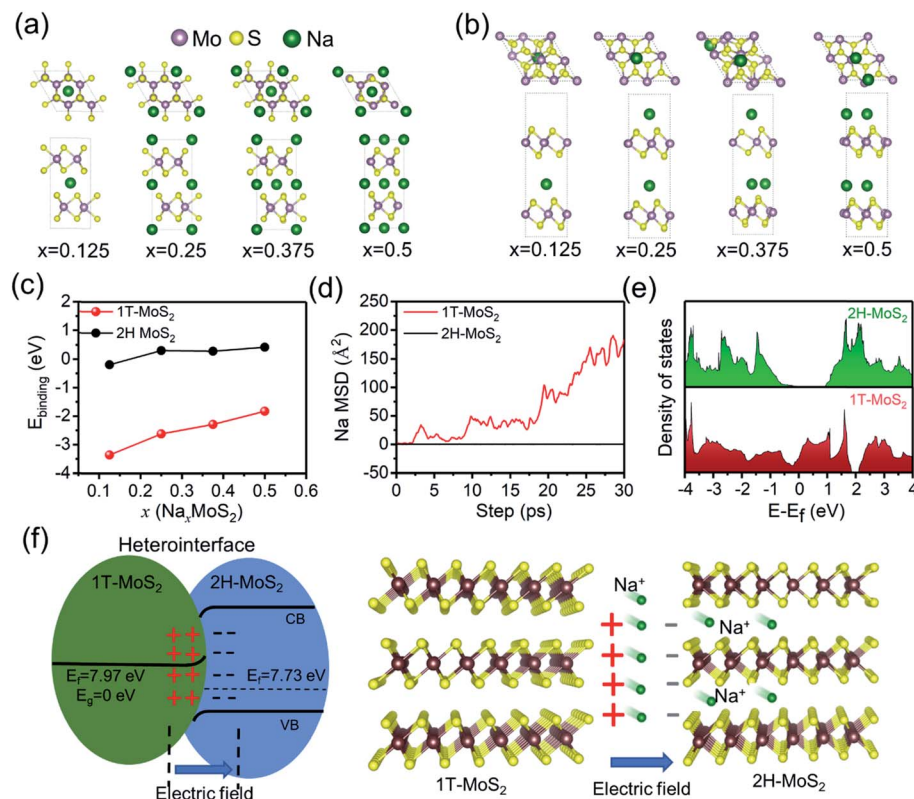


Fig. 5 Atomic structures of Na intercalated in (a) 2H-MoS₂ and (b) 1T-MoS₂; (c) binding energies of Na atoms in expanded 1T-MoS₂ and 2H-MoS₂; (d) Na MSD and (e) DOS of 1T-MoS₂ and 2H-MoS₂. (f) Schematic illustration of the formation mechanism and direction of the built-in electric field at the 1T- and 2H-MoS₂ heterointerface.

from 1 to 4 to form Na_xMoS₂ (with $x = 0.125, 0.25, 0.375$, and 0.5). The optimized atomic structures of Na⁺ intercalated 1T-MoS₂ and 2H-MoS₂ are shown in Fig. 5a and b, respectively. The binding energies of Na_xMoS₂ were consistently lower for 1T-MoS₂ than 2H-MoS₂ by more than 2.5 eV, as shown in Fig. 5c, suggesting a much higher Na affinity of 1T-MoS₂. The MSD values determined by AIMD simulations are shown in Fig. 5d. The diffusivity of Na⁺ in 1T-MoS₂ was consistently higher than in 2H-MoS₂, as evidenced by the large MSD values over the whole range of steps, in agreement with the GITT and EIS

results. The metallic nature of the density of states (DOS) plotted in Fig. 5e theoretically confirms the enhanced electronic conductivity of 1T-MoS₂. In summary, the simulation results support the enhanced electrical conductivity, higher Na affinity and higher Na⁺ mobility of 1T-MoS₂, which are responsible for the improved electrochemical performance of DP-MoS₂ in view of the predominance of the 1T phase. In addition, the difference in Fermi energy between the 1T- and the 2H-MoS₂ could induce an internal electric field at the corresponding heterointerface, see Fig. 5f.^{67–69} The electrostatic potential intrinsically built

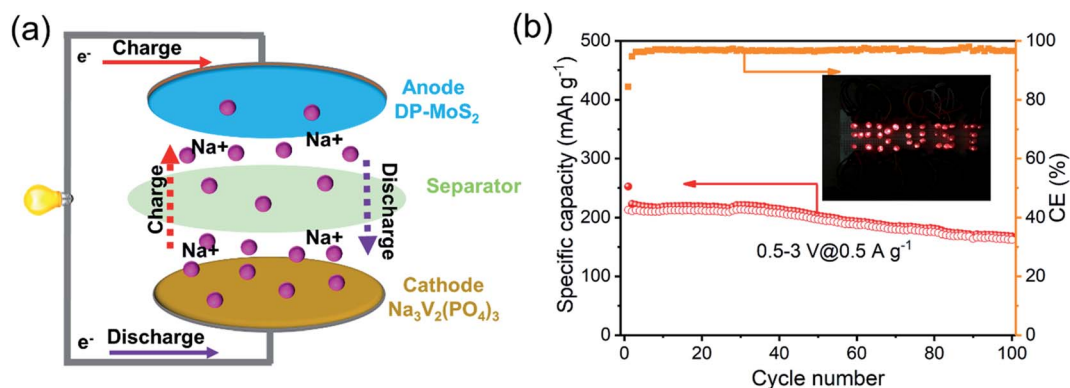


Fig. 6 (a) Schematic illustration of the DP-MoS₂//NVP full cell; (b) cyclic performance of the DP-MoS₂//NVP full cell at a current density of 0.5 A g⁻¹. The inset shows the LED array powered by the full battery.

between the 1T- and 2H-MoS₂ phases could attract the Na⁺ towards the 2H-MoS₂ side, promoting the migration of Na⁺. In addition, Jiang *et al.* reported that the formation of 1T-2H heterointerfaces can improve the overall electrical conductivity of the hybrid, while the integration of 2H phase is beneficial to stabilize 1T phase and ensure the durability of 1T/2H MoS₂ material.^{70,71}

3.4 Full-cell performance

To verify potential application of the DP-MoS₂ electrode, full cells (DP-MoS₂//NVP) were assembled using the DP-MoS₂ anode and an NVP cathode, as illustrated in Fig. 6a. The XRD pattern and SEM image of the NVP cathode are shown in Fig. S10.† The cells were first activated at 0.2 A g⁻¹ for 3 cycles, followed by testing at 0.5 A g⁻¹ in the following 100 cycles. Fig. S11† shows the GCD curves of the full cell at 0.5 A g⁻¹, delivering a high reversible capacity of ~213 mA h g⁻¹ in the operation window of 0.5–3 V. It maintained a high specific capacity of 168 mA h g⁻¹ after 100 cycles with capacity retention of ~80%, as shown in Fig. 6b. These values are superior to previous reports of NMF//NVP full cell,⁷² MoSe₂/rGO//NVP full cell,⁷³ and NVPF//SnS/G full cell.⁷⁴ The potential of the full cell in real-world applications was partly proven by powering a light-emitting diode (LED) array, see the inset of Fig. 6b.

4. Conclusion

We have synthesized DP-MoS₂ with expanded interlayer distance by a facile solvothermal method. As confirmed by the experimental results and DFT calculations, the expanded interlayer spacing and the predominance of the 1T phase significantly improved the electrical conductivity and enhanced the Na⁺ diffusivity of DP-MoS₂ compared to the common 2H-MoS₂. The DP-MoS₂ electrode delivered a high reversible capacity of 300 mA h g⁻¹ after 200 cycles at 0.5 A g⁻¹ in the potential range of 0.4–3.0 V. Furthermore, full cells were assembled by pairing the DP-MoS₂ anode with an NVP cathode and demonstrated stable cyclic performance at 0.5 A g⁻¹ for 100 cycles. The preparation approach and excellent electrochemical performance signify promising potential applications of DP-MoS₂ as an anode for SIBs.

Conflicts of interest

The authors declared that they have no conflicts of interest in this work.

Acknowledgements

This project was financially supported by the Research Grants Council (GRF Projects: 16207615, 16227016, 16204517, and 16208718) and the Innovation and Technology Commission (ITF projects ITS/001/17 and ITS/292/18FP) of Hong Kong SAR as well as the Guangzhou Science and Technology Program (No. 201807010074). The authors also appreciate the technical assistance from the Advanced Engineering Materials facilities

(AEMF) and the Materials Characterization and Preparation Facilities (MCPF) of HKUST.

References

- 1 G. Assat and J.-M. Tarascon, *Nat. Energy*, 2018, **3**, 373–386.
- 2 Z.-L. Xu, X. Liu, Y. Luo, L. Zhou and J.-K. Kim, *Prog. Mater. Sci.*, 2017, **90**, 1–44.
- 3 B. Li, Y. Yan, C. Shen, Y. Yu, Q. Wang and M. Liu, *Nanoscale*, 2018, **10**, 16217–16230.
- 4 M. Liu, Z. Yang, H. Sun, C. Lai, X. Zhao, H. Peng and T. Liu, *Nano Res.*, 2016, **9**, 3735–3746.
- 5 M. Liu, Y. Liu, Y. Yan, F. Wang, J. Liu and T. Liu, *Chem. Commun.*, 2017, **53**, 9097–9100.
- 6 H. Pan, Y.-S. Hu and L. Chen, *Energy Environ. Sci.*, 2013, **6**, 2338–2360.
- 7 N. Yabuuchi, K. Kubota, M. Dahbi and S. Komaba, *Chem. Rev.*, 2014, **114**, 11636–11682.
- 8 J. Cui, S. Yao and J.-K. Kim, *Energy Storage Mater.*, 2017, **7**, 64–114.
- 9 D. Sun, D. Ye, P. Liu, Y. Tang, J. Guo, L. Wang and H. Wang, *Adv. Energy Mater.*, 2018, **8**, 1702383.
- 10 J. W. Choi and D. Aurbach, *Nat. Rev. Mater.*, 2016, **1**, 16013.
- 11 P. Li, J. Y. Jeong, B. Jin, K. Zhang and J. H. Park, *Adv. Energy Mater.*, 2018, **8**, 1703300.
- 12 S. Yao, J. Cui, Z. Lu, Z. L. Xu, L. Qin, J. Huang, Z. Sadighi, F. Ciucci and J.-K. Kim, *Adv. Energy Mater.*, 2017, **7**, 1602149.
- 13 Q. Yun, L. Li, Z. Hu, Q. Lu, B. Chen and H. Zhang, *Adv. Mater.*, 2019, **31**, 1903826.
- 14 Q. Yun, Q. Lu, X. Zhang, C. Tan and H. Zhang, *Angew. Chem., Int. Ed.*, 2018, **57**, 626–646.
- 15 X. Wang, Q. Weng, Y. Yang, Y. Bando and D. Golberg, *Chem. Soc. Rev.*, 2016, **45**, 4042–4073.
- 16 Z. Hu, L. Wang, K. Zhang, J. Wang, F. Cheng, Z. Tao and J. Chen, *Angew. Chem., Int. Ed.*, 2014, **126**, 13008–13012.
- 17 C. Cui, Z. Wei, J. Xu, Y. Zhang, S. Liu, H. Liu, M. Mao, S. Wang, J. Ma and S. Dou, *Energy Storage Mater.*, 2018, **15**, 22–30.
- 18 J. Wu, Z. Lu, K. Li, J. Cui, S. Yao, M. Ihsan-ul Haq, B. Li, Q.-H. Yang, F. Kang, F. Ciucci and J.-K. Kim, *J. Mater. Chem. A*, 2018, **6**, 5668–5677.
- 19 Z.-H. Zhao, X.-D. Hu, H. Wang, M.-Y. Ye, Z.-Y. Sang, H.-M. Ji, X.-L. Li and Y. Dai, *Nano Energy*, 2018, **48**, 526–535.
- 20 C. Zhao, C. Yu, B. Qiu, S. Zhou, M. Zhang, H. Huang, B. Wang, J. Zhao, X. Sun and J. Qiu, *Adv. Mater.*, 2018, **30**, 1702486.
- 21 G. Liu, J. Cui, R. Luo, Y. Liu, X. Huang, N. Wu, X. Jin, H. Chen, S. Tang, J.-K. Kim and X. M. Liu, *Appl. Surf. Sci.*, 2019, **469**, 854–863.
- 22 M. Liu, P. Zhang, Z. Qu, Y. Yan, C. Lai, T. Liu and S. Zhang, *Nat. Commun.*, 2019, **10**, 3917.
- 23 R. Wang, S. Wang, Y. Zhang, D. Jin, X. Tao and L. Zhang, *Nanoscale*, 2018, **10**, 11165–11175.
- 24 X. Geng, Y. Zhang, Y. Han, J. Li, L. Yang, M. Benamara, L. Chen and H. Zhu, *Nano Lett.*, 2017, **17**, 1825–1832.
- 25 Y. Jiao, A. Mukhopadhyay, Y. Ma, L. Yang, A. M. Hafez and H. Zhu, *Adv. Energy Mater.*, 2018, **8**, 1702779.

- 26 P. Xiong, R. Ma, N. Sakai, L. Nurdiwijayanto and T. Sasaki, *ACS Energy Lett.*, 2018, **3**, 997–1005.
- 27 D. Sun, D. Huang, H. Wang, G.-L. Xu, X. Zhang, R. Zhang, Y. Tang, D. A. El-Hady, W. Alshitari and A. S. AL-Bogami, *Nano Energy*, 2019, **61**, 361–369.
- 28 X. Geng, Y. Jiao, Y. Han, A. Mukhopadhyay, L. Yang and H. Zhu, *Adv. Funct. Mater.*, 2017, **27**, 1702998.
- 29 M. Acerce, D. Voiry and M. Chhowalla, *Nat. Nanotechnol.*, 2015, **10**, 313–318.
- 30 Q. Liu, Q. Fang, W. Chu, Y. Wan, X. Li, W. Xu, M. Habib, S. Tao, Y. Zhou and D. Liu, *Chem. Mater.*, 2017, **29**, 4738–4744.
- 31 S. Wang, D. Zhang, B. Li, C. Zhang, Z. Du, H. Yin, X. Bi and S. Yang, *Adv. Energy Mater.*, 2018, **8**, 1801345.
- 32 Z. Sadighi, J. Liu, L. Zhao, F. Ciucci and J.-K. Kim, *Nanoscale*, 2018, **10**, 22549–22559.
- 33 S. S. Chou, Y.-K. Huang, J. Kim, B. Kaehr, B. M. Foley, P. Lu, C. Dykstra, P. E. Hopkins, C. J. Brinker and J. Huang, *J. Am. Chem. Soc.*, 2015, **137**, 1742–1745.
- 34 W. Chen, J. Gu, Q. Liu, R. Luo, L. Yao, B. Sun, W. Zhang, H. Su, B. Chen and P. Liu, *ACS Nano*, 2017, **12**, 308–316.
- 35 J. Zheng, H. Zhang, S. Dong, Y. Liu, C. T. Nai, H. S. Shin, H. Y. Jeong, B. Liu and K. P. Loh, *Nat. Commun.*, 2014, **5**, 2995.
- 36 D. Wang, Y. Xiao, X. Luo, Z. Wu, Y.-J. Wang and B. Fang, *ACS Sustainable Chem. Eng.*, 2017, **5**, 2509–2515.
- 37 Q. Liu, X. Li, Q. He, A. Khalil, D. Liu, T. Xiang, X. Wu and L. Song, *Small*, 2015, **11**, 5556–5564.
- 38 W. Ding, L. Hu, J. Dai, X. Tang, R. Wei, Z. Sheng, C. Liang, D. Shao, W. Song and Q. Liu, *ACS Nano*, 2019, **13**, 1694–1702.
- 39 G. Kresse and J. Furthmüller, *Phys. Rev. B: Condens. Matter Mater. Phys.*, 1996, **54**, 11169–11186.
- 40 J. P. Perdew, K. Burke and M. Ernzerhof, *Phys. Rev. Lett.*, 1996, **77**, 3865.
- 41 S. Grimme, J. Antony, S. Ehrlich and H. Krieg, *J. Chem. Phys.*, 2010, **132**, 154104.
- 42 S. Gong, G. Zhao, P. Lyu and K. Sun, *J. Mater. Chem. A*, 2019, **7**, 1187–1195.
- 43 J. Wu, J. Liu, Z. Lu, K. Lin, Y.-Q. Lyu, B. Li, F. Ciucci and J.-K. Kim, *Energy Storage Mater.*, 2019, **23**, 8–16.
- 44 J. Liu, Z. Lu, M. B. Effat and F. Ciucci, *J. Power Sources*, 2019, **409**, 94–101.
- 45 Y. Zhang, Z. Mu, C. Yang, Z. Xu, S. Zhang, X. Zhang, Y. Li, J. Lai, Z. Sun and Y. Yang, *Adv. Funct. Mater.*, 2018, **28**, 1707578.
- 46 M. Wu, J. Zhan, K. Wu, Z. Li, L. Wang, B. Geng, L. Wang and D. Pan, *J. Mater. Chem. A*, 2017, **5**, 14061–14069.
- 47 X. Xie, T. Makaryan, M. Zhao, K. L. Van Aken, Y. Gogotsi and G. Wang, *Adv. Energy Mater.*, 2016, **6**, 1502161.
- 48 Z.-T. Shi, W. Kang, J. Xu, Y.-W. Sun, M. Jiang, T.-W. Ng, H.-T. Xue, D. Y. W. Yu, W. Zhang and C.-S. Lee, *Nano Energy*, 2016, **22**, 27–37.
- 49 X. Geng, W. Sun, W. Wu, B. Chen, A. Al-Hilo, M. Benamara, H. Zhu, F. Watanabe, J. Cui and T.-P. Chen, *Nat. Commun.*, 2016, **7**, 10672.
- 50 Y. Jiao, A. M. Hafez, D. Cao, A. Mukhopadhyay, Y. Ma and H. Zhu, *Small*, 2018, **14**, 1800640.
- 51 A. Ejigu, I. A. Kinloch, E. Prestat and R. A. Dryfe, *J. Mater. Chem. A*, 2017, **5**, 11316–11330.
- 52 W. Ren, H. Zhang, C. Guan and C. Cheng, *Adv. Funct. Mater.*, 2017, **27**, 1702116.
- 53 Y. Li, Y. Liang, F. C. Robles Hernandez, H. Deog Yoo, Q. An and Y. Yao, *Nano Energy*, 2015, **15**, 453–461.
- 54 H. Xue, D. Y. W. Yu, J. Qing, X. Yang, J. Xu, Z. Li, M. Sun, W. Kang, Y. Tang and C.-S. Lee, *J. Mater. Chem. A*, 2015, **3**, 7945–7949.
- 55 L. Pan, X.-D. Zhu, X.-M. Xie and Y.-T. Liu, *Adv. Funct. Mater.*, 2015, **25**, 3341–3350.
- 56 W. Han, X. Qin, J. Wu, Q. Li, M. Liu, Y. Xia, H. Du, B. Li and F. Kang, *Nano Res.*, 2017, **11**, 892.
- 57 G. Jia, D. Chao, N. H. Tiep, Z. Zhang and H. Fan, *Energy Storage Mater.*, 2018, **14**, 136–142.
- 58 R. Wang, S. Wang, X. Peng, Y. Zhang, D. Jin, P. K. Chu and L. Zhang, *ACS Appl. Mater. Interfaces*, 2017, **9**, 32745–32755.
- 59 X. Wang, S. Kajiyama, H. Iinuma, E. Hosono, S. Oro, I. Moriguchi, M. Okubo and A. Yamada, *Nat. Commun.*, 2015, **6**, 6544.
- 60 Y. Wen, K. He, Y. Zhu, F. Han, Y. Xu, I. Matsuda, Y. Ishii, J. Cumings and C. Wang, *Nat. Commun.*, 2014, **5**, 4033.
- 61 Y. Li, Y.-S. Hu, M.-M. Titirici, L. Chen and X. Huang, *Adv. Energy Mater.*, 2016, **6**, 1600659.
- 62 Y. Niu, M. Xu, Y. Zhang, J. Han, Y. Wang and C. M. Li, *RSC Adv.*, 2016, **6**, 45605–45611.
- 63 Q. Wang, X. Zhu, Y. Liu, Y. Fang, X. Zhou and J. Bao, *Carbon*, 2018, **127**, 658–666.
- 64 H. Li, Y. Wang, J. Jiang, Y. Zhang, Y. Peng and J. Zhao, *Electrochim. Acta*, 2017, **247**, 851–859.
- 65 C. W. Mason, I. Gocheva, H. E. Hoster and Y. Denis, *Chem. Commun.*, 2014, **50**, 2249–2251.
- 66 E. Quattrocchi, T. H. Wan, A. Curcio, S. Pepe, M. B. Effat and F. Ciucci, *Electrochim. Acta*, 2019, **324**, 134853.
- 67 C. Zhang, F. Han, F. Wang, Q. Liu, D. Zhou, F. Zhang, S. Xu, C. Fan, X. Li and J. Liu, *Energy Storage Mater.*, 2020, **24**, 208–219.
- 68 C. Zhang, F. Han, J. Ma, Z. Li, F. Zhang, S. Xu, H. Liu, X. Li, J. Liu and A.-H. Lu, *J. Mater. Chem. A*, 2019, **7**, 11771–11781.
- 69 L. Fang, Z. Lan, W. Guan, P. Zhou, N. Bahlawane, W. Sun, Y. Lu, C. Liang, M. Yan and Y. Jiang, *Energy Storage Mater.*, 2019, **18**, 107–113.
- 70 L. Jiang, S. Zhang, S. A. Kulinich, X. Song, J. Zhu, X. Wang and H. Zeng, *Mater. Res. Lett.*, 2015, **3**, 177–183.
- 71 D. Wang, X. Zhang, S. Bao, Z. Zhang, H. Fei and Z. Wu, *J. Mater. Chem. A*, 2017, **5**, 2681–2688.
- 72 P. Tao, J. He, T. Shen, Y. Hao, J. Yan, Z. Huang, X. Xu, M. Li and Y. Chen, *Adv. Mater. Interfaces*, 2019, **6**, 1900460.
- 73 Z. Liu, Y. Zhang, H. Zhao, N. Li and Y. Du, *Sci. China Mater.*, 2017, **60**, 167–177.
- 74 Y. C. Lu, C. Ma, J. Alvarado, N. Dimov, Y. S. Meng and S. Okada, *J. Mater. Chem. A*, 2015, **3**, 16971–16977.